RSC Advances

PAPER

View Article Online
View Journal | View Issue

Cite this: *RSC Adv.*, 2019, **9**, 1990

Microstructural analysis, magnetic properties, magnetocaloric effect, and critical behaviors of $Ni_{0.6}Cd_{0.2}Cu_{0.2}Fe_2O_4$ ferrites prepared using the sol–gel method under different sintering temperatures

Noura Kouki,[ab] Sobhi Hcini,[*c] Michel Boudard,[d] Reema Aldawas[a] and Abdessalem Dhahri[e]

This work focuses on the microstructural analysis, magnetic properties, magnetocaloric effect, and critical exponents of $Ni_{0.6}Cd_{0.2}Cu_{0.2}Fe_2O_4$ ferrites. These samples, denoted as S1000 and S1200, were prepared using the sol–gel method and sintered separately at 1000 °C and 1200 °C, respectively. XRD patterns confirmed the formation of cubic spinel structures and the Rietveld method was used to estimate the different structural parameters. The higher sintering temperature led to an increased lattice constant (*a*), crystallite size (*D*), magnetization (*M*), Curie temperature (T_C), and magnetic entropy change ($-\Delta S_M$) for samples that exhibited second-order ferromagnetic–paramagnetic (FM–PM) phase transitions. The magnetic entropy changed at an applied magnetic field ($\mu_0 H$) of 5 T, reaching maximum values of about 1.57–2.12 J kg^{-1} K^{-1}, corresponding to relative cooling powers (RCPs) of 115 and 125 J kg^{-1} for S1000 and S1200, respectively. Critical exponents (β, γ, and δ) for samples around their T_C values were studied by analyzing the $M(\mu_0 H, T)$ isothermal magnetizations using different techniques and checked by analyzing the $-\Delta S_M$ *vs.* $\mu_0 H$ curves. The estimated values of β and γ exponents (using the Kouvel–Fisher method) and δ exponent (from $M(T_C, \mu_0 H)$ critical isotherms) were $\beta = 0.443 \pm 0.003$, $\gamma = 1.032 \pm 0.001$, and $\delta = 3.311 \pm 0.006$ for S1000, and $\beta = 0.403 \pm 0.008$, $\gamma = 1.073 \pm 0.016$, and $\delta = 3.650 \pm 0.005$ for S1200. Obviously, these critical exponents were affected by an increased sintering temperature and their values were different to those predicted by standard theoretical models.

Received 3rd November 2018
Accepted 31st December 2018

DOI: 10.1039/c8ra09113g

rsc.li/rsc-advances

1. Introduction

Magnetic refrigeration (MR) is an alternative technology to refrigeration based on the conventional vapor cycle technique.[1] Owing to its economic and environmental benefits, especially its energy efficiency, magnetic refrigeration is a promising technique for the future of refrigeration. Therefore, the equivalent of a conventional thermodynamic cycle can be realized magnetically with better energy efficiency and without greenhouse gases. Objectives in this area are the synthesis, optimization, and implementation of materials with high magnetocaloric power that are effective, economical, ecological, and practical for medium term implementation in pilot refrigeration systems. MR is based on the magnetocaloric effect (MCE), which is an intrinsic thermodynamic property of magnetic materials that causes a change in the temperature of the substance under the action of a magnetic field. Gadolinium (Gd) is a rare earth metal with a Curie temperature (T_C) close to room temperature. Gd is the only pure metallic magnetic material that has a high MCE around its Curie temperature (T_C = 293 K).[2,3] Although Gd is the first choice for academic MR research near room temperature, its use is commercially limited owing to its high price (~4000 $ per kg) and easy oxidation. In recent years, large MCEs have been found in other materials, such as perovskite manganites ABO_3 (ref. 4–8) and spinel ferrites AFe_2O_4,[9–14] which have attracted increasing attention in MR research. The main advantages of these materials over Gd and GdSiGe alloys[15] are low coercive forces, nonactive chemical properties (no oxidation), low costs, and high electric resistance (minimum Eddy current loss).[16] Spinel ferrites have been studied less than perovskite materials in the field of MR. Accordingly, in this study, we have prepared ferrite samples with $Ni_{0.6}Cd_{0.2}Cu_{0.2}Fe_2O_4$ compositions using the sol–gel method at sintering temperatures of 1000 °C and 1200 °C. We

[a]*Department of Chemistry, College of Science and Arts, Qassim University, Buraydah, Saudi Arabia*

[b]*Laboratory of Water, Membranes and Environment Biotechnology (EMBE), Technopole of Borj Cedria (CERTE), 2050 Hammam Lif, Tunisia*

[c]*Faculty of Science and Technology of Sidi Bouzid, Research Unit of Valorization and Optimization of Exploitation of Resources, University Campus Agricultural City, University of Kairouan, 9100 Sidi Bouzid, Tunisia. E-mail: hcini_sobhi@yahoo.fr*

[d]*LMGP, University of Grenoble Aples, CNRS, 38000 Grenoble, France*

[e]*Department of Physics, Laboratory of Physical Chemistry of Materials, Faculty of Science of Monastir, University of Monastir, 5019, Monastir, Tunisia*

then investigated the effect of sintering temperature on their microstructural, magnetic, and magnetocaloric properties. Finally, a detailed study of critical exponents near their Curie temperatures (T_C) was conducted using varies techniques, such as modified Arrott plots, the Kouvel–Fisher method, and critical isotherm analysis. Throughout this manuscript, we have used the abbreviations S1000 and S1200 to denote $Ni_{0.6}Cd_{0.2}Cu_{0.2}Fe_2O_4$ ferrites sintered at 1000 °C and 1200 °C, respectively.

2. Experimental details

2.1. Synthetic process

$Ni_{0.6}Cd_{0.2}Cu_{0.2}Fe_2O_4$ ferrites were synthesized from $[Ni(NO_3)_2 \cdot 6H_2O]$, $[Cd(NO_3)_2 \cdot 4H_2O]$, $[Cu(NO_3)_2 \cdot 3H_2O]$ and $[Fe(NO_3)_3 \cdot 9H_2O]$ nitrates using the sol–gel method, the main steps of which are shown in Fig. 1. Stoichiometric amounts of nitrates were first dissolved in distilled water with regular stirring at

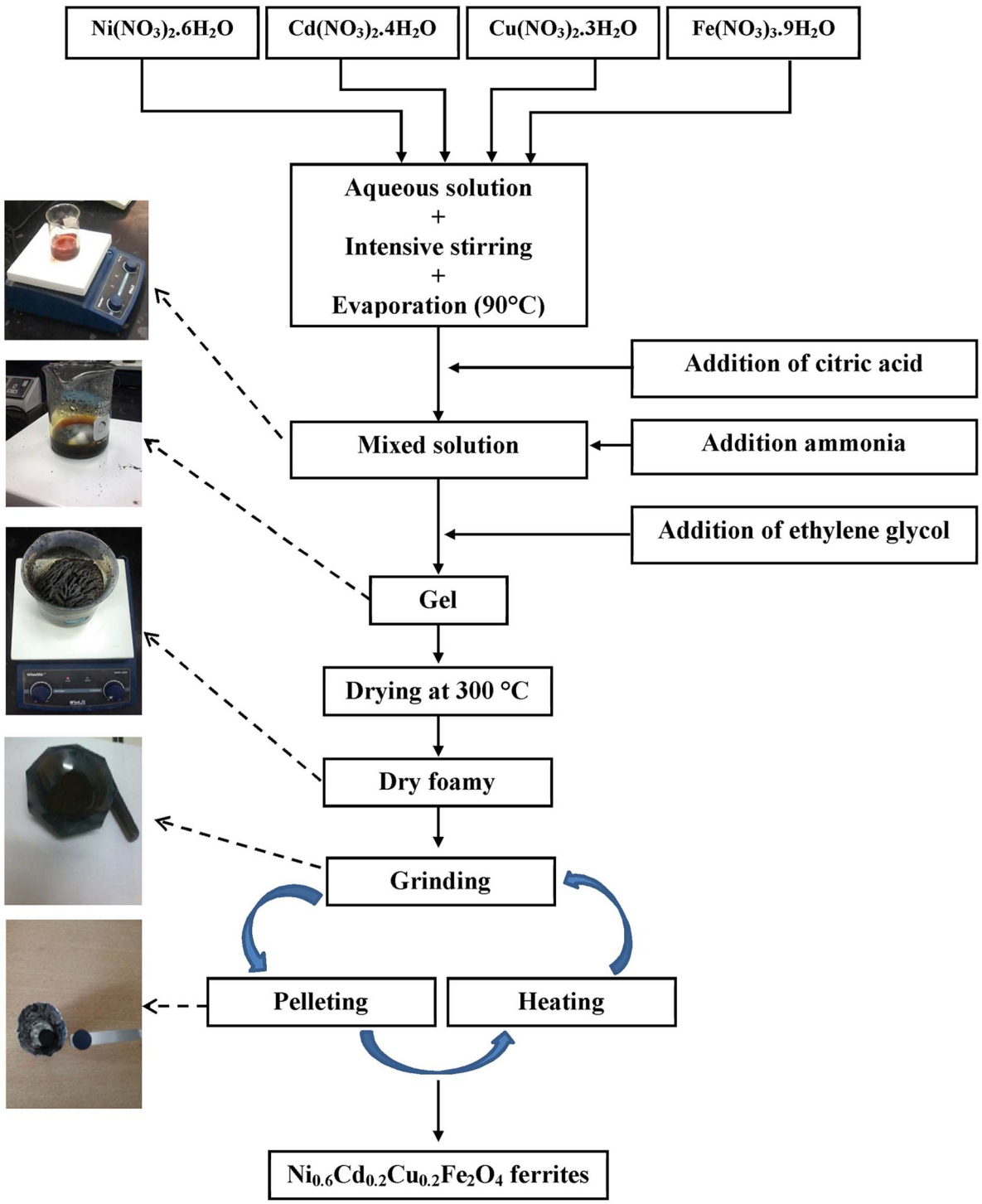

Fig. 1 Schematic diagram representing the various synthesis steps for S1000 and S1200 samples using the sol–gel method.

90 °C on a hot plate. Controlled quantities of citric acid, used as a complexation agent, were added to the mixed solution. The solution pH was adjusted to about 7 by adding ammonia. Stoichiometric amounts of ethylene glycol, used as a polymerization agent, were then added to the solution. Heating and stirring were continued until gel formation after approximately 4 h. The gel was dried at 300 °C for 6 h to obtain a dry foam, which was then ground in a mortar and further dried at 500 °C for 12 h in air. The resulting powder was pressed into pellets (diameter, 10 mm; thickness, about 2 mm) and sintered at 700 °C for 12 h. Finally, the powder was ground and pressed again, and divided into two portions, which were sintered separately for 24 h at 1000 °C and 1200 °C, respectively.

2.2. Characterization

A PANalytical X'Pert Pro diffractometer using Ni-filtered CuK_α radiation ($\lambda = 1.5406$ Å) was used to record X-ray diffraction patterns in the angular range of 20–80°. Rietveld analysis[17] using FullProf software was adopted for detailed structural characterization. The free surface morphologies of samples in pellet form were analyzed by scanning electron microscopy (SEM) using a Philips XL30 microscope under an accelerating voltage of 15 kV. A linear extraction magnetometer was used to record the temperature and magnetic field dependences of the magnetization. $M(T)$ curves were measured in the temperature range 300 K $\leq T \leq$ 750 K under a constant magnetic field ($\mu_0 H = 0.05$ T), and $M(\mu_0 H, T)$ isotherms were taken at different temperatures near T_C in the magnetic field range 0 T $\leq \mu_0 H \leq$ 5 T.

3. Results and discussions

3.1. Microstructural analysis

3.1.1. XRD patterns. XRD patterns of S1000 and S1200 are shown in Fig. 2. Analysis of these patterns confirmed that both samples had cubic spinel structures with a $Fd\bar{3}m$ space group. Furthermore, no additional peaks related to phase impurities were detected, confirming the sample purity. As shown in the inset of Fig. 2, the XRD patterns showed a shift in the most intense peak (311) position to lower diffraction angles (2θ) with increasing sintering temperature. This indicated that the lattice constant changed with increasing sintering temperature. The compound structures were refined to $Fd\bar{3}m$ symmetry, accounting for the cation distributions $(Cd^{2+}_{0.2}Fe^{3+}_{0.8})_A[Ni^{2+}_{0.6}Cu^{2+}_{0.2}Fe^{3+}_{1.2}]_BO^{2-}_4$. The distributions of Cd^{2+}, Ni^{2+}, Cu^{2+}, and Fe^{3+} ions were proposed based on literature precedent.[18–21] The atomic positions were fixed at 8a (1/8, 1/8, 1/8) for $(Cd^{2+}_{0.2}Fe^{3+}_{0.8})_A$ cations, 16d (1/2, 1/2, 1/2) for $[Ni^{2+}_{0.6}Cu^{2+}_{0.2}Fe^{3+}_{1.2}]_B$ cations, and 32e (x, y, z) for O. Refinements of all parameters were continued until the value of the quality factor, χ^2 (goodness of fit), was close to unity, which confirmed the goodness of the refinement (Fig. 3). The lattice constant (a), volume (V), cation–oxygen distances in A and B sites (R_A and R_B), average crystallite size (D), and intensity ratio (I_{220}/I_{222}) were obtained from Rietveld refinement, as summarized in Table 1. The results clearly indicated that the lattice parameters

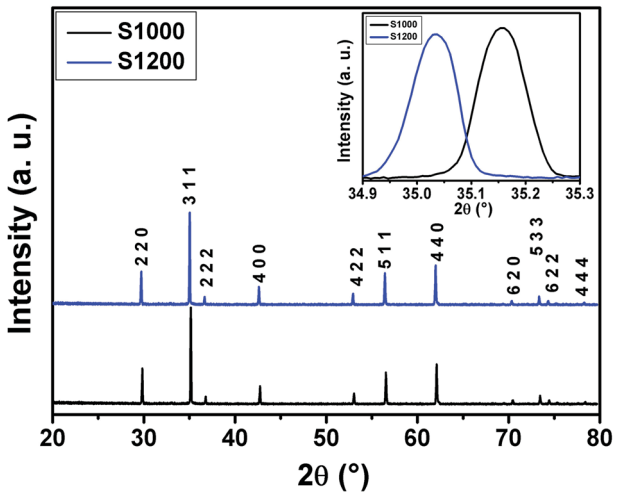

Fig. 2 XRD patterns of S1000 and S1200 samples. All peaks of the manganite phase are indexed to cubic spinel $Fd\bar{3}m$ symmetry. Inset shows the observed XRD profiles of the most intense peak (Bragg reflections 311).

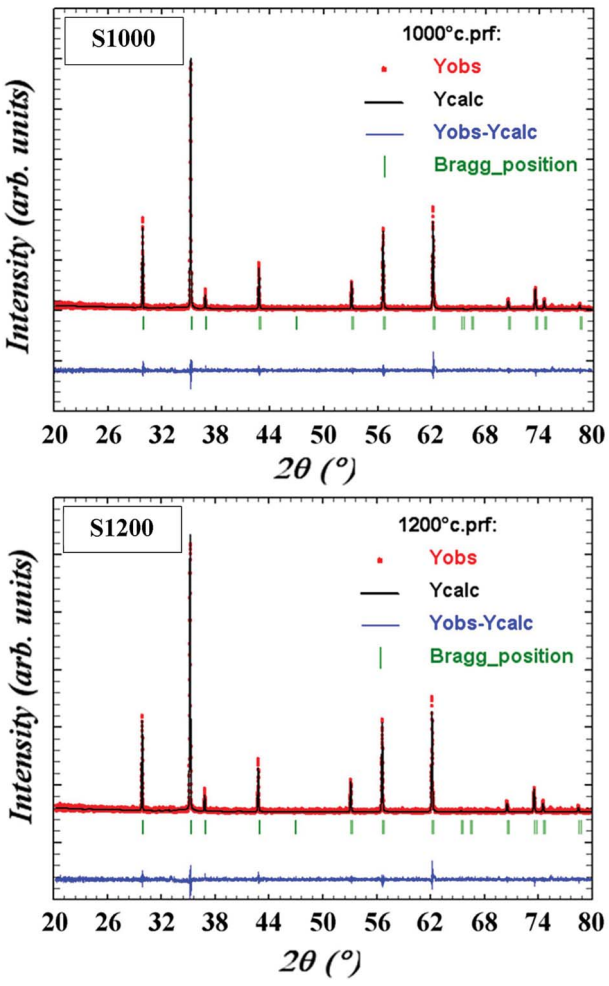

Fig. 3 Rietveld analysis of XRD patterns for S1000 and S1200. Bottom line (blue) represents the difference between the XRD data (red) and calculated fit (black); green lines are Bragg positions. All peaks are indexed to the cubic spinel-type structure ($Fd\bar{3}m$ space group).

Table 1 Structural parameters obtained from the Rietveld refinement of S1000 and S1200[a]

Samples				S1000	S1200
Space group				$Fd\bar{3}m$	
Lattice parameters	a (Å)			8.4382 (3)	8.4421 (2)
	V (Å^3)			600.83 (3)	601.67 (2)
Atoms	Cd/Fe$_1$	Wyckoff positions		4c	4c
		Site symmetry		−43m	−43m
		Atomic positions	$x = y = z$	1/8	1/8
		B_{iso} (Å^2)		0.64 (1)	1.10 (1)
	Ni/Cu/Fe$_2$	Wyckoff positions		16d	16d
		Site symmetry		−3m	−3m
		Atomic positions	$x = y = z$	1/2	1/2
		B_{iso} (Å^2)		1.11 (1)	1.29 (1)
	O	Wyckoff positions		32e	32e
		Site symmetry		3m	3m
		Atomic positions	$x = y = z$	0.2601 (9)	0.2541 (9)
		B_{iso} (Å^2)		2.18 (9)	1.41 (2)
Structural parameters	R_A (Å)			1.963(8)	1.946(11)
	R_B (Å)			2.038(8)	2.030(8)
	I_{220}/I_{222}			3.91	4.42
	D (μm)			0.122	0.138
Agreement factors	R_p (%)			20.1	21.8
	R_{wp} (%)			29.9	31.4
	R_F (%)			10.4	13.2
	χ^2 (%)			1.24	1.47

[a] Numbers in parentheses are estimated standard deviations to the last significant digit. B_{iso}, the isotropic Debye–Waller factor. Structural parameters a, V, R_A, R_B, D, and I_{220}/I_{222} are defined in the text. Agreement factors of profile R_p, weighted profile R_{wp}, and structure R_F. χ^2, goodness of fit.

increased, while the R_A and R_B distances decreased, with increasing sintering temperature. This was in agreement with the results of previous studies.[22,23] Furthermore, the obtained oxygen coordinate values were characteristic of a spinel-type structure.[24,25] The average crystallite sizes of the samples were obtained from XRD peaks using the Scherrer equation:[22]

$$D = \frac{0.9\lambda}{\beta \cos(\theta)} \quad (1)$$

where λ is the X-ray wavelength, θ is the diffraction angle of the most intense peak (311), and β is its full width at half maximum (FWHM). β must be corrected according to the following formula:

$$\beta = \sqrt{{\beta_x}^2 - {\beta_{instr}}^2} \quad (2)$$

where β_x is the experimental FWHM and β_{instr} is the FWHM of a standard silicon sample. The estimated values of average crystallite sizes are summarized in Table 1. The D values clearly increased with increasing sintering temperature, in good agreement with previous reports.[22,23] The intensity ratio (I_{220}/I_{222}) values are also shown in Table 1. The intensity of the (220) and (222) planes depends on the cation distribution in the tetrahedral (A) and octahedral sites (B), respectively.[26] The calculated values increased with increasing sintering temperature, indicating that the degree of inversion† was reduced with increasing sintering temperature.[27]

† Inversion is defined as the fraction of A sites occupied by Fe^{3+} cations and its value depends on the method of preparation and heat treatment effects.[27]

3.1.2. SEM images. SEM micrographs of S1000 and S1200 are shown in Fig. 4. For both samples, the micrographs exhibited regular shaped grains, most with spherical morphology, while S1200 grains were significantly larger than those of S1000. Analysis of the SEM images using Image J software showed average particle sizes of about 0.180 and 0.412 μm for S1000 and S1200, respectively. Therefore, the SEM images confirmed the increase in particles size with increasing sintering temperature. The tendency of particles to join together and produce large particles with negligible porosity was evident in S1200. These observations were consistent with the XRD results, but the crystallite sizes estimated from XRD peaks were clearly smaller than the particle sizes obtained from SEM micrographs. This difference was attributed to the particles being composed of several crystallites, which caused internal strains or defects in the structure.[5]

3.2. Magnetic properties

Variations in the magnetization (M) with temperature (T) under a magnetic field of 0.05 T for S1000 and S1200 samples are shown in Fig. 5. Clear ferromagnetic–paramagnetic (FM–PM) phase transitions were observed for both samples at their Curie temperatures (T_C). T_C values were determined, accounting for the minimum values of (dM/dT *vs.* T) curves, which are given in the insets of Fig. 5. The T_C values increased from 655 K to 680 K for S1000 and S1200, respectively. Furthermore, at the higher sintering temperature, the magnetization amplitude in the FM region also increased. The increments in both M and T_C values with increasing sintering temperature can be related to the

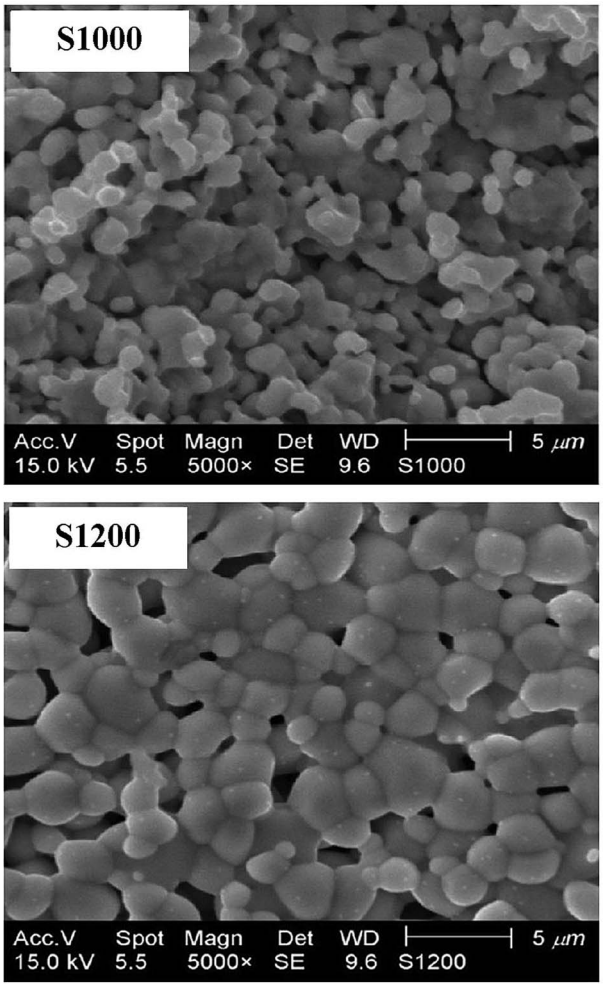

Fig. 4 SEM micrographs of S1000 and S1200.

increase in crystallite size. Furthermore, according to the core/surface morphology, the spin arrangement on the surface is lower than that in the core. The surface is considered a magnetically dead layer, with the randomly disordered. Therefore, as the crystallite size increases with increasing sintering temperature, this nonmagnetic surface layer decreases and, consequently, the core/shell thickness ratio increases. This leads to the elimination of surface effects (broken exchange bonds, spin canting) and, therefore, an improvement in both M and T_C values was observed.[23] This result can also be interpreted in another way by considering variation in the degree of inversion parameter.[27,28] According to the XRD results, the degree of inversion was reduced with increasing sintering temperature. The decreased degree of inversion would cause the average exchange interaction between Fe^{3+} ions in tetrahedral and octahedral sites to increase, which resulted in an increase in the M and T_C values.[28] This explained why the as-prepared S1000 sample with a higher inversion degree had lower M and T_C values, while the S1200 sample with a low inversion degree had higher M and T_C values.

3.3. Magnetocaloric properties

Fig. 6 shows the $M(\mu_0 H, T)$ isothermal magnetizations taken near the T_C values of S1000 and S1200. The nature of the magnetic phase transitions of these samples was determined

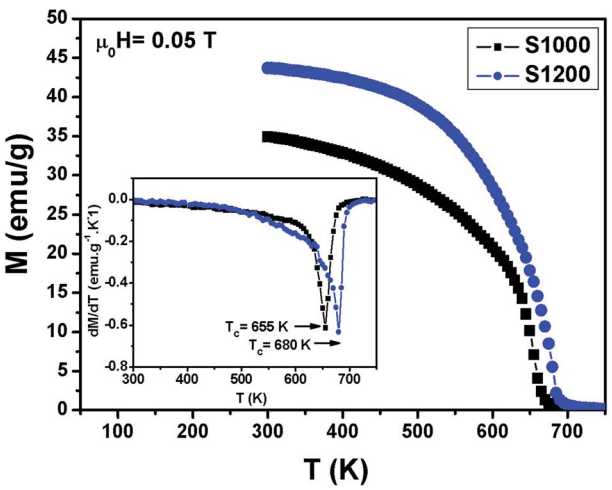

Fig. 5 Temperature dependence of magnetization measured at $\mu_0 H = 0.05$ T for S1000 and S1200. Insets are plots of dM/dT *vs.* T.

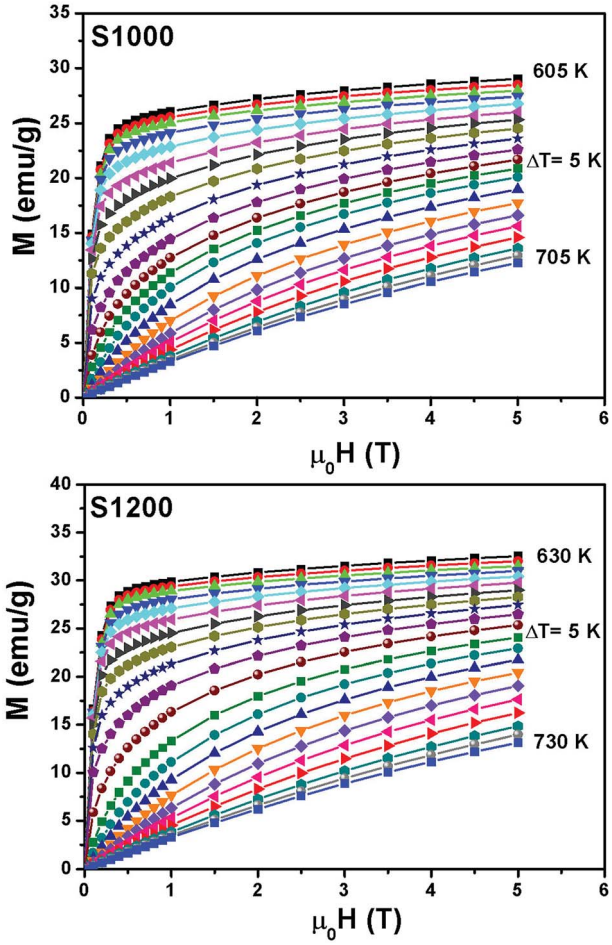

Fig. 6 Applied magnetic field dependence of magnetization at different temperatures $M(\mu_0 H, T)$ around the T_C values of S1000 and S1200.

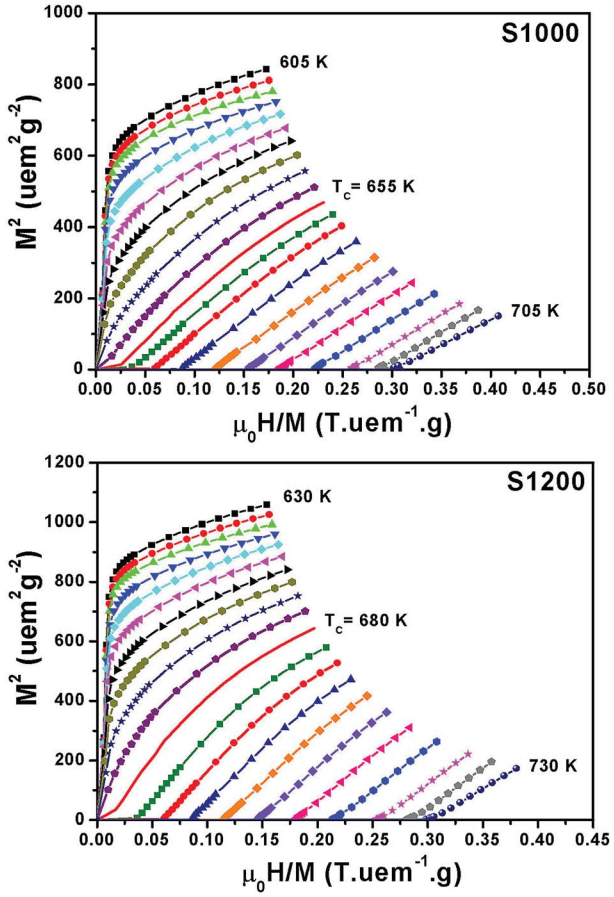

Fig. 7 Arrott plots (M^2 *vs.* μ_0H/M) near the T_C values of S1000 and S1200.

using Banerjee's criterion[29] and M^2 *vs.* μ_0H/M Arrott plots.[30] Fig. 7 shows the Arrott plots of both samples. Analysis of these plots showed that they have positive slopes around the T_C, which confirmed that the magnetic phase transitions were second-order. Using M (μ_0H, T) isotherms, the dependence of magnetic entropy change ($-\Delta S_M$) on temperature (T) was calculated according to the following Maxwell relation:[1]

$$\Delta S_M(T, \mu_0 H) = \sum \frac{M_i - M_{i+1}}{T_i - T_{i+1}} \Delta(\mu_0 H) \quad (3)$$

where M_i and M_{i+1} are the magnetization values at T_i and T_{i+1}, respectively, measured under the magnetic field (μ_0H). Fig. 8 shows the $-\Delta S_M(T, \mu_0H)$ curves for S1000 and S1200. These curves exhibited maximum peaks defined as the maximum magnetic entropy change ($-\Delta S_M^{max}$) near T_C. This resulted from the increase in the number of magnetic moments oriented in the direction of the applied magnetic field. The effectiveness of samples for magnetic refrigeration applications can be measured by calculating the relative cooling power (RCP) using the following equation:[1]

$$RCP = |\Delta S_M^{max}| \times \delta T_{FWHM} \quad (4)$$

where δT_{FWHM} is the fullwidth at $0.5\Delta S_M^{max}$. The magnetic field dependences of $-\Delta S_M^{max}$ and RCP obtained for S1000 and S1200 are shown in Table 2 and Fig. 9. Both increased linearly with an increasing magnetic field. Furthermore, the increase in sintering temperature led to an increase in the $-\Delta S_M^{max}$ values from 1.57 J kg^{-1} K^{-1} for S1000 to 2.12 J kg^{-1} K^{-1} for S1200 (at $\mu_0H = 5$ T). This variation in magnetic entropy change with increasing sintering temperature was in agreement with the results of previous studies.[31,32] The estimated RCP values were 115 and 125 J kg^{-1} for S1000 and S1200, respectively. These values were relatively high, indicating that the prepared samples are potential candidates for cooling power technology. Furthermore, the $-\Delta S_M^{max}$ and RCP values were comparable to those found at the same applied magnetic field in some other ferrite systems that are considered potential candidates for magnetic refrigeration.[9,11,14]

3.4. Critical behavior

3.4.1. Scaling. The critical behaviors of S1000 and S1200 near their Curie temperatures were analyzed by conducting a detailed study of their critical exponents (β, γ, and δ). According to Stanley's hypothesis,[33] the exponents β and γ can

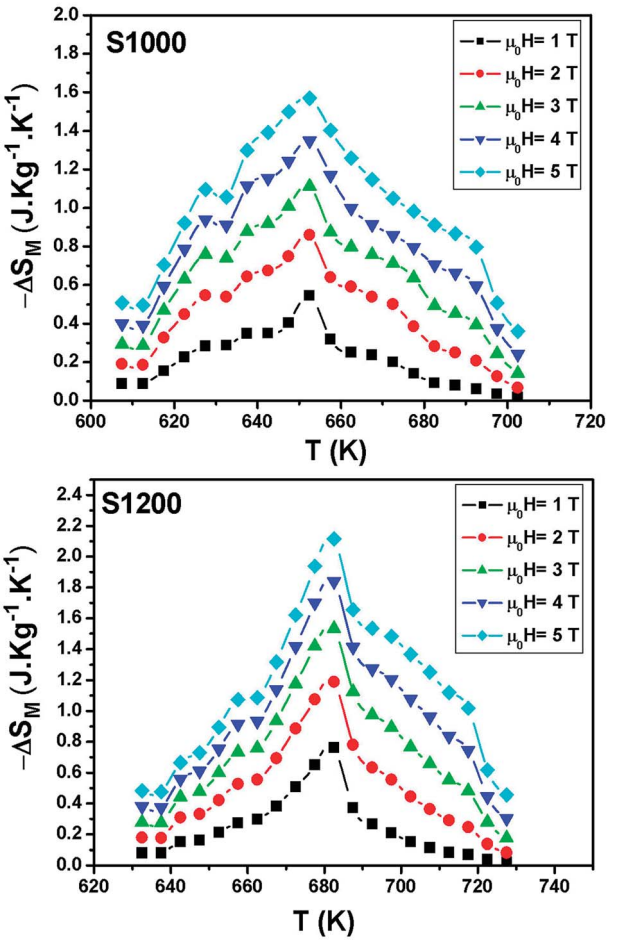

Fig. 8 Temperature and magnetic field dependences of the magnetic entropy change for S1000 and S1200.

Table 2 Magnetocaloric properties (at a magnetic field of 5 T) for S1000 and S1200 ferrites compared with those of other ferrite systems at the same applied magnetic field

Samples	T_C (K)	$\mu_0 H$ (T)	$\lvert\Delta S_M^{max}\rvert$ (J kg^{-1} K^{-1})	RCP (J kg^{-1})	Ref.
$Ni_{0.6}Cd_{0.2}Cu_{0.2}Fe_2O_4$ (1000 °C)	**655**	**5**	**1.57**	**115**	**Present work**
$Ni_{0.6}Cd_{0.2}Cu_{0.2}Fe_2O_4$ (1200 °C)	**680**	**5**	**2.12**	**125**	**Present work**
$Zn_{0.6}Cu_{0.4}Fe_2O_4$	305	5	1.16	289	9
$Zn_{0.4}Ni_{0.2}Cu_{0.4}Fe_2O_4$	565	5	1.41	141	9
$Zn_{0.2}Ni_{0.4}Cu_{0.4}Fe_2O_4$	705	5	1.61	233	9
$Cu_{0.4}Zn_{0.6}Fe_2O_4$	373	5	1.77	—	11
$Cu_{0.2}Zn_{0.8}Fe_2O_4$	140	5	1.17	—	11
$Ni_{0.4}Mg_{0.3}Cu_{0.3}Fe_2O_4$	690	5	1.56	136	14

be estimated r from the temperature dependence of spontaneous magnetization, M_s (below T_C), and the initial magnetic susceptibility, χ_0 (above T_C), respectively. Meanwhile, exponent δ can be deduced directly from the magnetic isotherm at $T = T_C$. These three critical exponents can be determined using the following equations:[33]

$$M_s(T) = M_0(-\varepsilon)^{\beta} \text{ (with } \varepsilon < 0 \text{ and } T < T_C) \quad (5)$$

$$\chi_0^{-1}(T) = \left(\frac{h_0}{M_0}\right)\varepsilon^{\gamma} \text{(with } \varepsilon > 0 \text{ and } T > T_C) \quad (6)$$

$$M = D(\mu_0 H)^{1/\delta} \text{ (with } \varepsilon = 0 \text{ and } T = T_C) \quad (7)$$

where ε is the reduced temperature ($\varepsilon = (T - T_C)/T_C$), and M_0, h_0/M_0, and D are the critical amplitudes. According to Stanley's scaling hypothesis, the magnetic state equation in the critical region is:[33]

$$M(\mu_0 H, \varepsilon) = |\varepsilon|^{\beta} f_{\pm}\left(\frac{\mu_0 H}{|\varepsilon|^{\beta+\gamma}}\right) \quad (8)$$

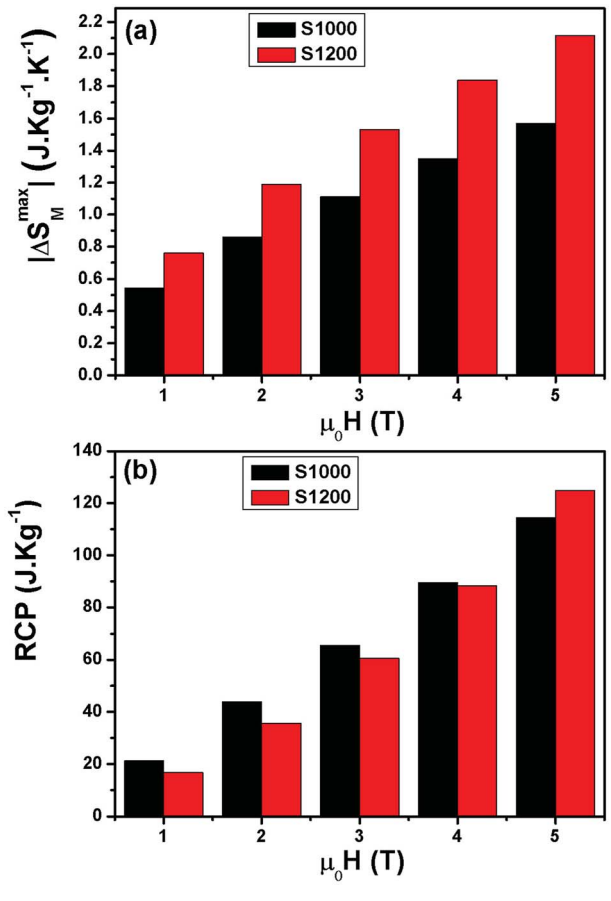

Fig. 9 (a) Magnetic field dependence of maximum magnetic entropy change $-\Delta S_M^{max}$ and (b) relative cooling power values (RCP) of S1000 and S1200.

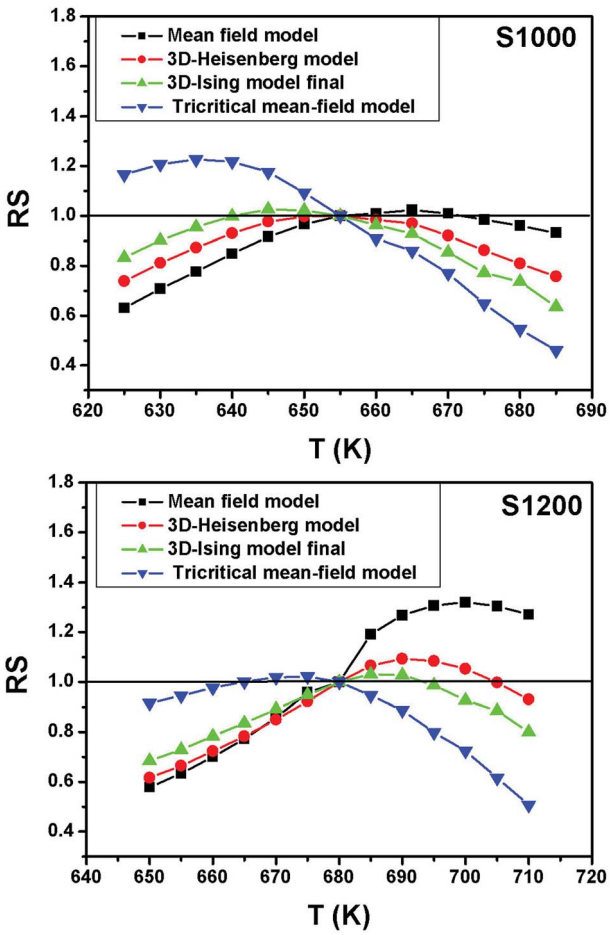

Fig. 10 Relative slope (RS) *vs.* temperature deduced from the four theoretical models for S1000 and S1200.

where f_+ and f_- are regular analytical functions defined at the ($T > T_C$) and ($T < T_C$) regions, respectively. For a better estimation of β and γ critical exponents, this equation implies that $M|\varepsilon|^{-\beta}$ *vs.* $\mu_0 H|\varepsilon|^{-(\beta+\gamma)}$ curves can be divided along two universal branches (one for $T < T_C$ and another for $T > T_C$).

3.4.2. Analysis. According to the mean field model, the Arrott plots (M^2 *vs.* $\mu_0 H/M$) shown in Fig. 7 should give a series of straight lines in the high-field region at different temperatures around T_C, and the line at T_C should cross the origin.[33] As shown in Fig. 7, these conditions were not accurate, which indicated that the mean field model was invalid to describe the critical behaviors of S1000 and S1200. Therefore, to obtain the correct β and γ critical exponents for the samples, the $M(\mu_0 H, T)$ isotherms were analyzed using the modified Arrott plots (MAP) by representing $M^{1/\beta}$ *vs.* $(\mu_0 H/M)^{1/\gamma}$ curves.[34] Notably, the MAP gave more importance to data in the region of high magnetic fields compared to those in the weak-field region. Three theoretical models are generally applied to estimate β, γ, and δ exponents, as follows:[35,36] (i) the 3D Heisenberg model with $\beta = 0.365$, $\gamma = 1.336$, and $\delta = 4.8$; (ii) the 3D Ising model with $\beta = 0.325$, $\gamma = 1.24$, and $\delta = 4.82$; and (iii) the tricritical mean-field model with $\beta = 0.25$, $\gamma = 1$, and $\delta = 5$. In our case, we first used these three models to construct MAPs (not presented in this work) for S1000 and S1200, and then, from each MAP, calculated the relative slope (RS), which is defined as:

$$\mathrm{RS} = \frac{S(T)}{S(T_C)} \tag{9}$$

For the best theoretical model, the RS values should be close to unity, mainly because the MAPs are series of parallel isotherms.[37] Fig. 10 shows the values of RS *vs.* T corresponding to each model. For both samples, the RS values were clearly higher than unity. This suggested that the theoretical models were not useful for estimating the critical exponents of the prepared samples. Therefore, we concluded that the samples had unconventional critical exponents. This motivated us to construct new MAPs. We attempted to find new critical exponent values until we obtained parallel isotherms at around T_C, and the isotherm of $M^{1/\beta}$ *vs.* $(\mu_0 H/M)^{1/\gamma}$ at T_C crossed the origin. These conditions were reached with values of $\beta = 0.444$ and $\gamma = 1.031$ for S1000, and $\beta = 0.408$ and $\gamma = 1.075$ for S1200 (Fig. 11). Linear extrapolation of the experimental data in Fig. 11 allowed determination of the spontaneous magnetization, M_s (below T_C), by intersection with the $M^{1/\beta}$ axis and the initial magnetic susceptibility values, χ_0^{-1} (above T_C), by intersection with the $(\mu_0 H/M)^{1/\gamma}$ axis. The $M_s(T)$ and $\chi_0(T)$ data were then adjusted using the eqn (5) and (6), respectively. During this adjustment, new values of β and γ were obtained simultaneously. The T_C

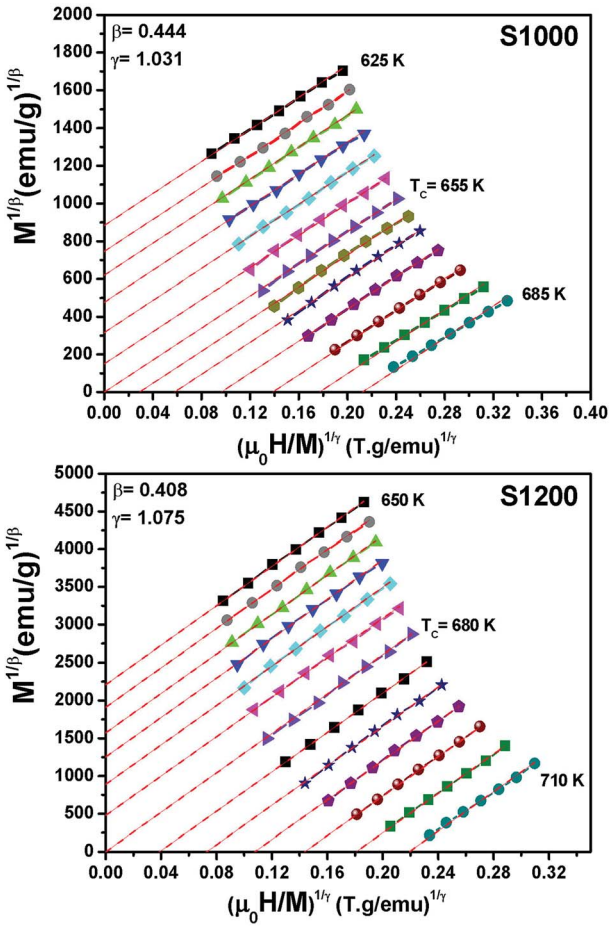

Fig. 11 Modified Arrott plots ($M^{1/\beta}$ *vs.* $(\mu_0 H/M)^{1/\gamma}$) with reliable critical exponents obtained for S1000 and S1200.

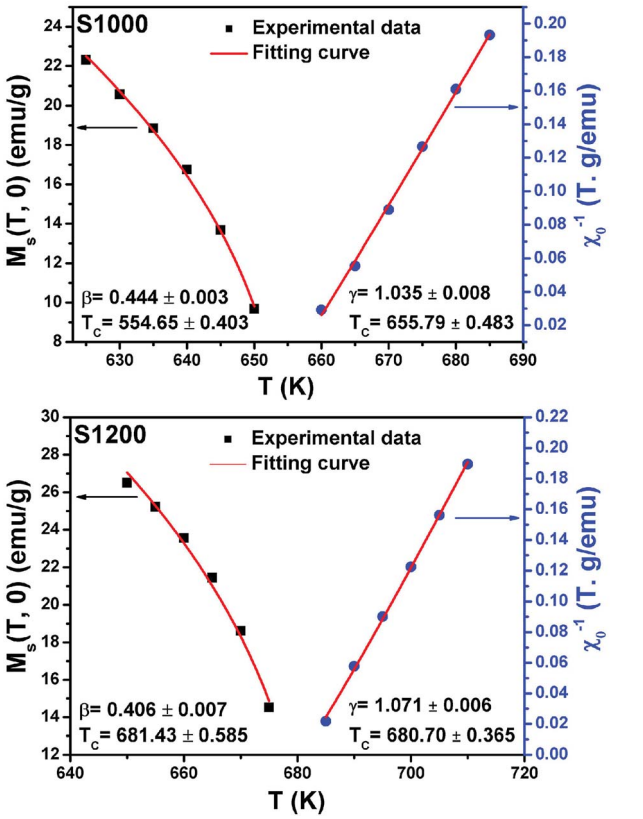

Fig. 12 Spontaneous magnetization $M_s(T)$ (left axis) and inverse initial susceptibility $\chi_0^{-1}(T)$ (right axis) of S1000 and S1200. Red solid lines are the fits according to eqn (5) and (6), respectively.

value associated with each curve was also determined. After several adjustment tests, the values of β, γ, and T_C converged toward their optimal values. As shown in Fig. 12, the theoretical and experimental curves were in good agreement. The obtained values shown in Fig. 12 also agreed well with those presented in Fig. 11. The β, γ, and T_C values were also determined more precisely using the Kouvel–Fisher method using the following two equations:[38,39]

$$M_s(T)\left[\frac{dM_s(T)}{dT}\right]^{-1} = \frac{(T - T_C)}{\beta} \quad (10)$$

$$\chi_0^{-1}(T)\left[\frac{d\chi_0^{-1}(T)}{dT}\right]^{-1} = \frac{(T - T_C)}{\gamma} \quad (11)$$

Linear adjustment of $M_s(T)\left[\frac{dM_s(T)}{dT}\right]^{-1}$ *vs.* T gave a slope equal to $1/\beta$, while the linear adjustment of $\chi_0^{-1}(T)\left[\frac{d\chi_0^{-1}(T)}{dT}\right]^{-1}$ *vs.* T gave a slope equal to $1/\gamma$. These curves are shown in Fig. 13. The red lines represent the best adjustments using eqn (10) and (11). The obtained values of β, γ, and T_C parameters shown in Fig. 13 were consistent with those used in Fig. 11. The variation in the critical isotherm $M(T_C, \mu_0 H)$ can be described by a power law characterized by the critical exponent δ. This exponent can be obtained by adjusting $M(T_C, \mu_0 H)$ curve in log–log scale using eqn (7), as shown in Fig. 14. From this adjustment, it was possible to determine the slope of the curve $(1/\delta)$ and consequently the values of δ (see Fig. 14). The three critical exponents, β, γ, and δ, determined previously can be related, according to statistical theory, to the Widom relation:[40]

$$\delta = 1 + \frac{\gamma}{\beta} \quad (12)$$

By replacing β and γ in this equation with the values shown in Fig. 12 and 13, eqn (12) gave δ values of 3.331 and 3.329 for S1000, and 3.638 and 3.662 for S1200. These values were very close to those estimated from the critical isotherm at T_C, as shown in Fig. 14 (δ = 3.311 and 3.650 for S1000 and S1200, respectively). These results implied that the values of β, γ, and δ were well determined. Variation in the term $(M|\varepsilon|^{-\beta})$ *vs.* $(\mu_0 H|\varepsilon|^{-(\beta+\gamma)})$ according to eqn (8) is plotted in Fig. 15 using the β and γ values previously obtained by the Kouvel–Fisher method for some temperatures below and above the T_C. Fig. 15 shows the superposition of all curves along two separate branches for $(T < T_C)$ and $(T > T_C)$, respectively, which suggested that the obtained values of critical exponents and those for T_C

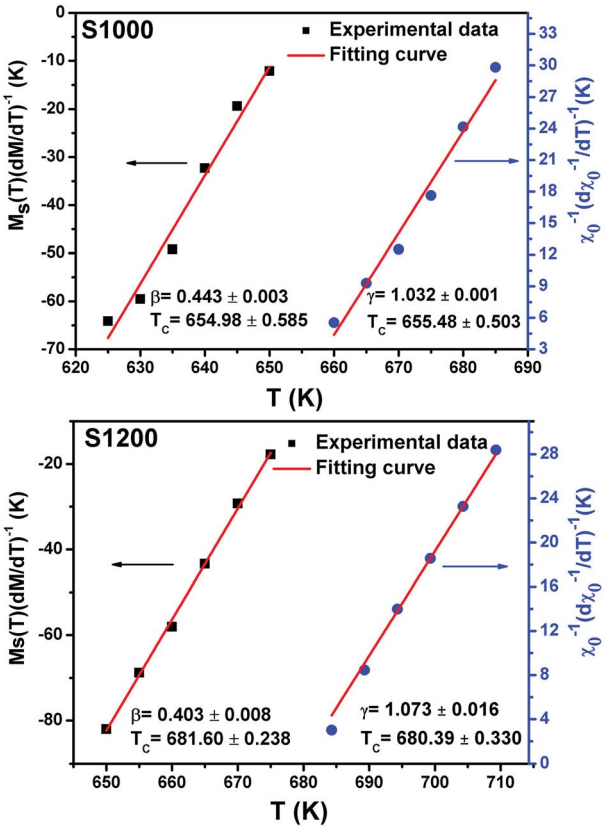

Fig. 13 Kouvel–Fisher plots for spontaneous magnetization $M_s(T)$ (left axis) and inverse initial susceptibility $\chi_0^{-1}(T)$ (right axis) of S1000 and S1200. Red solid lines are the fits according to eqn (10) and (11), respectively.

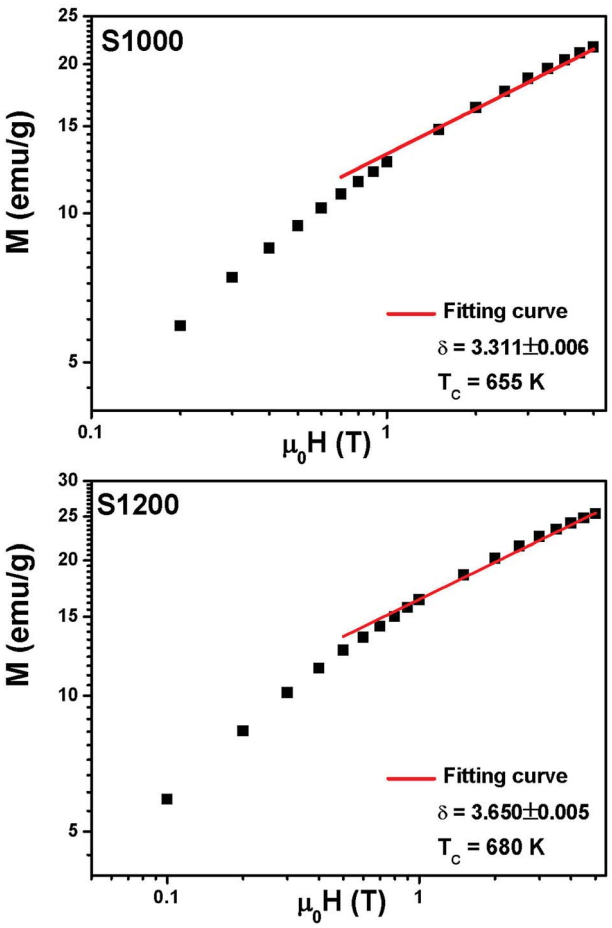

Fig. 14 $M(T_C, \mu_0 H)$ isotherms in the log–log scale for S1000 and S1200. Red solid lines are the linear fit according to eqn (7).

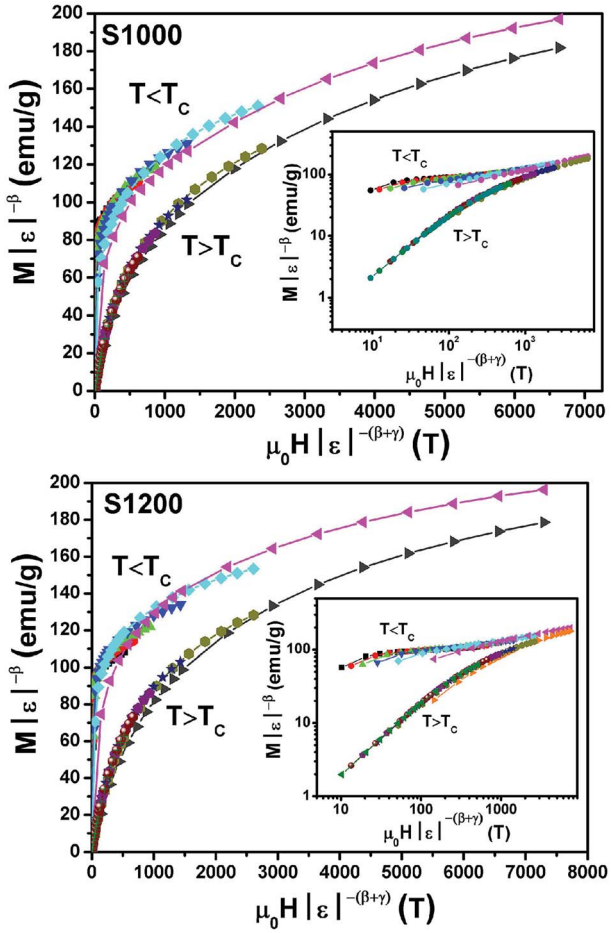

Fig. 15 Scaling plots for S1000 and S1200 below and above T_C values using β and γ estimated using the Kouvel–Fisher method. Insets show plots in the log–log scale.

were reasonably precise. The insets of Fig. 15 also show the variation in these curves on the log–log scale. A linear superposition was observed at higher magnetic fields in the curves in the two regions (below and above T_C), while the setting of the curves to the log–log scale became especially bad in the weak fields (some bifurcations of the curves were observed in different directions). This confirmed that this scale theory gives much more importance to data in higher fields than those in weak fields.

The influence of the critical exponents on the MCE can be demonstrated by analyzing the variation in the magnetic entropy change with magnetic field according to following power law:[41]

$$|\Delta S_M^{max}| = a(\mu_0 H)^n \quad (13)$$

where a is a constant and n is an exponent that depends on the magnetic state of the samples. In this particular case, at $T = T_C$, the n exponent becomes independent of the magnetic field.[42] Therefore:

$$n(T_C) = 1 + \frac{\beta - 1}{\beta + \gamma} \quad (14)$$

where β and γ are the critical exponents. By multiplying the Widom relation by β, we can write $\beta\delta = (\beta + \gamma)$, and consequently eqn (14) can be rewritten as:

$$n = 1 + \frac{1}{\delta}\left(1 - \frac{1}{\beta}\right) \quad (15)$$

By considering the values of β and γ obtained from the Kouvel–Fisher method, and the values of δ obtained from the $M(T_C, H)$ critical isotherms, the n values calculated from the previous relations were:

From eqn (14):

$$\begin{cases} n = 622 \text{ for sample sintered at } 1000\ ^\circ\text{C} \\ n = 0.596 \text{ for samples sintered at } 1200\ ^\circ\text{C} \end{cases}$$

From eqn (15):

$$\begin{cases} n = 0.620 \text{ for sample sintered at } 1000\ ^\circ\text{C} \\ n = 0.594 \text{ for sample sintered at } 1200\ ^\circ\text{C} \end{cases}$$

The n values can also be estimated by fitting the $|\Delta S_M^{max}|$ *vs.* $\mu_0 H$ curve at T_C according to eqn (13), as shown in Fig. 16. The fitting curves gave n values of 0.626 and 0.601 for S1000 and S1200, respectively. These values were in good agreement with those obtained from eqn (14) and (15). This suggested that the critical exponents obtained for the studied samples were reliable. The obtained values of the critical exponents of S1000 and S1200 (present work) are compared with the predicted values of the four theoretical models in Table 3.[35,36] We found that β and δ exponents lay between the mean field model and the 3D Heisenberg model, while the δ values were close to that of the mean field model. However, as the sintering temperature increased, the critical exponent β decreased, while γ and δ exponents increased. The decreasing β exponent reflected a faster growth of the ordered moment with increasing sintering temperature. However, the deviation of this exponent from the mean field model was attributed to the presence of an inhomogeneous magnetic state in the samples.[43,44]

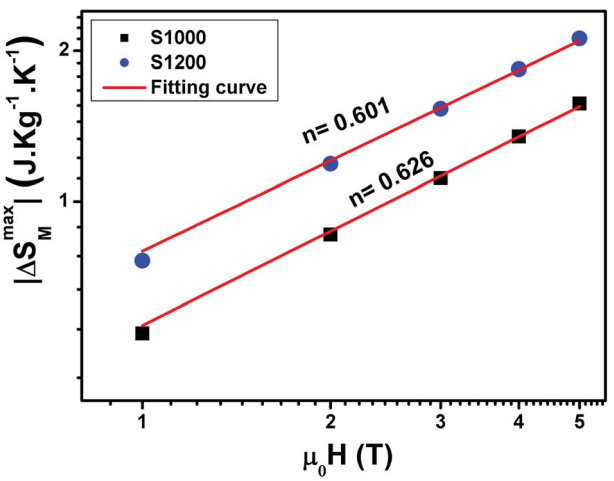

Fig. 16 Magnetic field dependence of $|\Delta S_M^{max}|$ at T_C fitted to the power law $|\Delta S_M^{max}| = a(\mu_0 H)^n$ for S1000 and S1200.

Table 3 Comparison of the critical exponent values of S1000 and S1200 (present work) with those predicted by the standard theoretical models

Material	Technique	T_C (K)	β	γ	δ	Ref.
Mean-field model			0.5	1.0	3.0	35
3D Heisenberg model			0.365 ± 0.003	1.336 ± 0.004	4.80 ± 0.04	35
3D Ising model			0.325 ± 0.002	1.24 ± 0.002	4.82 ± 0.02	35
Tricritical mean-field model			0.25	1.0	5.0	36
$Ni_{0.6}Cd_{0.2}Cu_{0.2}Fe_2O_4$ (1000 °C)	Modified Arrott plots	55.65 ± 0.403	0.444 ± 0.003	—	—	Present work
		655.79 ± 0.483	—	1.035 ± 0.008	—	
	Kouvel–Fisher method	654.98 ± 0.585	0.443 ± 0.003	—	—	
		655.48 ± 0.503	—	1.032 ± 0.001	—	
	Critical isotherm	—	—	—	3.311 ± 0.006	
$Ni_{0.6}Cd_{0.2}Cu_{0.2}Fe_2O_4$ (1200 °C)	Modified Arrott plots	681.43 ± 0.585	0.406 ± 0.007	—	—	Present work
		680.70 ± 0.365	—	1.071 ± 0.006	—	
	Kouvel–Fisher method	681.60 ± 0.238	0.403 ± 0.008	—	—	
		680.39 ± 0.330	—	1.073 ± 0.016	—	
	Critical isotherm	—	—	—	3.650 ± 0.005	

4. Conclusion

The sol–gel method was used to prepare $Ni_{0.6}Cd_{0.4}Cu_{0.2}Fe_2O_4$ ferrites at sintering temperatures of 1000 °C and 1200 °C. XRD patterns and Rietveld refinements confirmed that the samples had cubic spinel type structures. Magnetic measurements showed that the samples presented second-order FM–PM phase transitions with increasing magnetization amplitude and Curie temperature when the sintering temperature was increased. The values of maximum magnetic entropy change and relative cooling power were relatively high and comparable to those of some other ferrite systems considered potential candidates for magnetic refrigeration. This showed that the prepared samples were useful for cooling power technology. Critical exponents β, γ, and δ were determined using different methods. These exponents belonged to a different universality class, with exponent β decreasing and exponents γ and δ increasing with increasing sintering temperature.

Conflicts of interest

There are no conflicts to declare.

Acknowledgements

The authors gratefully acknowledge Qassim University, represented by the Deanship of Scientific Research, for material support of this research under the grant number 5090-cosabu-2018-1-14-S during academic year 2018.

References

1 M. H. Phan and S. C. Yu, *J. Magn. Magn. Mater.*, 2007, **308**, 325.
2 G. V. Brown, *J. Appl. Phys.*, 1976, **47**, 3673.
3 M. Foldeaki, R. Chachine and T. K. Bose, *J. Appl. Phys.*, 1995, **77**(7), 3528.
4 S. Hcini, M. Boudard, S. Zemni and M. Oumezzine, *Ceram. Int.*, 2014, **40**, 16041.
5 E. Oumezzine, S. Hcini, E. K. Hlil, E. Dhahri and M. Oumezzine, *J. Alloys Compd.*, 2014, **615**, 553.
6 M. Iqbal, M. N. Khan, A. A. Khan and N. Zafar, *J. Alloys Compd.*, 2018, **769**, 766.
7 A. Elghoul, A. Krichene, N. C. Boudjada and W. Boujelben, *Ceram. Int.*, 2018, **44**, 12723.
8 R. Thaljaoui, M. Pękała, J.-F. Fagnard and Ph. Vanderbemden, *J. Rare Earths*, 2017, **35**, 875.
9 E. Oumezzine, S. Hcini, M. Baazaoui, E. K. Hlil and M. Oumezzine, *Powder Technol.*, 2015, **278**, 189.
10 M. S. Anwar, F. Ahmed and B. H. Koo, *Acta Mater.*, 2014, **71**, 100.
11 S. Akhter, D. P. Paul, S. M. Hoque, M. A. Hakim, M. Hudl, R. Mathieu and P. Nordblad, *J. Magn. Magn. Mater.*, 2014, **367**, 75.
12 A. A. Khan, U. Hira, Z. Iqbal, M. Usman and F. Sher, *Ceram. Int.*, 2017, **43**, 7088.
13 R. Felhi, H. Omrani, M. Koubaa, W. Cheikhrouhou Koubaa and A. Cheikhrouhou, *J. Alloys Compd.*, 2018, **758**, 237.
14 S. Hcini, N. Kouki, R. Aldawas, M. Boudard, A. Dhahri and M. L. Bouazizi, *J. Supercond. Novel Magn.*, 2018, DOI: 10.1007/s10948-018-4813-6.
15 V. K. Pecharsky and K. A. Gschneidner Jr, *Phys. Rev. Lett.*, 1997, **78**(23), 4494.
16 B. Anis, T. Samanta, S. Banerjee and I. Das, *Appl. Phys. Lett.*, 2008, **9**(2), 212502.
17 H. M. Rietveld, *J. Appl. Crystallogr.*, 1969, **2**, 65.
18 M. A. Hakim, S. K. Nath, S. S. Sikder and K. H. Maria, *J. Phys. Chem. Solids*, 2013, **74**, 1316.
19 K. S. Lohar, S. M. Patange, M. L. Mane and S. E. Shirsath, *J. Mol. Struct.*, 2013, **1032**, 105.
20 M. Houshiar and L. Jamilpanah, *Mater. Res. Bull.*, 2018, **98**, 213.
21 A. Gholizadeh and E. Jafari, *J. Magn. Magn. Mater.*, 2017, **422**, 328.
22 R. P. Patil, P. P. Hankare, K. M. Garadkar and R. Sasikala, *J. Alloys Compd.*, 2012, **523**, 66.
23 M. Rahimi, P. Kameli, M. Ranjbar and H. Salamati, *J. Nanopart. Res.*, 2013, **15**, 1865.

24 N. Pailhé, A. Wattiaux, M. Gaudon and A. Demourgues, *J. Solid State Chem.*, 2008, **181**, 1040.
25 K. Verma, A. Kumar and D. Varshney, *J. Alloys Compd.*, 2012, **526**, 91.
26 V. Sepelak, D. Baabe, D. Mienert, D. Schultze, F. Krumeich, F. J. Litterst and K. D. Becker, *J. Magn. Magn. Mater.*, 2003, **257**, 377.
27 G. Ahmad and J. Elahe, *J. Magn. Magn. Mater.*, 2017, **422**, 328.
28 Z. Zi, Y. Sun, X. Zhu, Z. Yang, J. Dai and W. Song, *J. Magn. Magn. Mater.*, 2009, **321**, 1251.
29 A. Arrott, *Phys. Rev.*, 1957, **108**, 1394.
30 S. K. Banerjee, *Phys. Lett.*, 1964, **12**, 16.
31 R. M'nassri, N. C. Boudjada and A. Cheikhrouhou, *J. Alloys Compd.*, 2015, **626**, 20.
32 S. R. Lee, M. S. Anwar, F. Ahmed and B. H. Koo, *Trans. Nonferrous Met. Soc. China*, 2014, **24**, s141.
33 H. E. Stanley, *Introduction to Phase Transitions and Critical Phenomena*, Oxford University Press, London, 1971.
34 A. Arrott and J. E. Noakes, *Phys. Rev. Lett.*, 1967, **19**, 786.
35 S. N. Kaul, *J. Magn. Magn. Mater.*, 1985, **53**, 5.
36 K. Huang, *Statistical Mechanics*, Wiley, New York, 2nd edn, 1987.
37 A. Schwartz, M. Scheffler and S. M. Anlage, *Phys. Rev. B: Condens. Matter Mater. Phys.*, 2000, **61**, R870.
38 M. E. Fisher, S. K. Ma and B. G. Nickel, *Phys. Rev. Lett.*, 1972, **29**, 917.
39 J. S. Kouvel and M. E. Fisher, *Phys. Rev.*, 1964, **136**, 1626.
40 B. Widom, *J. Chem. Phys.*, 1964, **41**, 1633.
41 Q. Y. Dong, H. W. Zhang, J. R. Sun, B. G. Shen and V. Franco, *J. Appl. Phys.*, 2008, **103**, 116101.
42 V. Franco, J. S. Blázquez and A. Conde, *Appl. Phys. Lett.*, 2006, **89**, 222512.
43 J. Fan, L. Ling, B. Hong, L. Zhang, L. Pi and Y. Zhang, *Phys. Rev. B: Condens. Matter Mater. Phys.*, 2010, **81**, 144426.
44 T. D. Thanh, Y. YiKyung, T. A. Ho, T. V. Manh, T. L. Phan, D. M. Tartakovsky and S. C. Yu, *IEEE Trans. Magn.*, 2015, **51**, 1.